An enriched shell element formulation for modeling of inter- and intralaminar crack propagation in laminates

Jim Brouzoulis[a], Martin Fagerström[a,*], Erik Svenning[a]

[a]*Department of Applied Mechanics*
Division of Material and Computational Mechanics
Chalmers University of Technology, Gothenburg, Sweden

Abstract

In traditional finite element modeling of progressive failure in laminated fiber reinforced polymers, inter- and intralaminar cracks are normally treated in different ways. Interlaminar cracks are normally described explicitly by building up the laminate using stacked elements (solids or shells) connected by cohesive interface elements. Intralaminar cracks, one the other hand, are more often accounted for by using a continuum damage approach, (e.g. a smeared crack approach). In this paper, we propose a modeling concept which instead can accurately represent both intralaminar and interlaminar cracks with an extended kinematical representation, whereby cracks can be explicitly accounted for without excessive use of degrees of freedom. With this concept, we aim to take one step closer to more efficient FE analyses of progressive laminate failure, since only one shell element through the thickness is required, and where arbitrary inter- and intralaminar crack propagation are accounted for only in areas where it is needed. We show that the current shell formulation proposed can be utilized to describe the kinematics of a laminate containing multiple inter- and intralaminar cracks. Thus, we see significant potential for this modeling concept in analyses in which computational efficiency is of major importance.

Keywords: multiple interlaminar cracks, multiple intralaminar cracks, XFEM, computational efficiency, shells

*Corresponding author. Address: Hörsalsvägen 7, SE–412 96 Göteborg, Sweden. E-mail:martin.fagerstrom@chalmers.se. Phone: +46 31 772 1300.

1. Introduction

The automotive industry is currently very active in reducing vehicle weight, where one significant step is to increase the amount of structural Fibre Reinforced Polymers (FRPs) due to their superior specific properties compared to conventional metals. However, for FRP materials to see widespread use in future cars, there are many challenges which yet remain to be resolved. One important challenge is to be able to assess and predict the crashworthiness of a car with load bearing and crash energy absorbing components made out of such structural composites. Crucial for the development of new car models with an increasing amount of structural composites is thereby to have reliable and computationally efficient crashworthiness assessment methods and material models, since the vehicle development process today is intensively driven by numerical simulation.

Experimentally, the crashworthiness of FRPs, or more specifically the energy absorption capability of these materials, has been analyzed by many authors, cf. *e.g.* the reviews by Carruthers *et al.* [1] and Jacob *et al.* [2]. From these studies, it can be concluded that for Carbon Fibre Reinforced Polymers (CFRPs) the specific energy absorption in axial compression can be higher or significantly higher compared to aluminium and steel grades used in crash structures today[1]. However, in the papers by Hull [5] and Grauers *et al.* [6] it is clear that this beneficial material characteristic is the consequence of a very complicated fracture process in the material involving many competing failure mechanisms, *e.g.* fiber kinking (and breaking) in compression, compressive matrix failure and significant (mixed-mode) delamination. From these observations, it is clear that to achieve accurate predictions of the crashworthiness performance of CFRP components in simulations, careful considerations of the underlying failure mechanisms are necessary for the proper modeling of the structural behavior.

Today, there are limited number of papers on the topic of material modeling of composites devoted specifically to crash accounting for large strains (and potentially high strain-rates) and including the relevant mechanisms listed above. There are however existing models with general application to progressive damage development, cf. *e.g.* Pinho *et al.* [7, 8], Maimi *et al.* [9]

[1] As an example, it is reported by Hamada *et al.* [3] that a Carbon Fibre–PEEK composite can be designed to yield twice as high specific energy absorption compared to Aluminium 6061 as reported by Farley [4].

and Gutkin and Pinho [10], the latter incorporating also frictional effects along the crack planes, which could be utilized and/or adopted for crash applications.

But in addition to the accuracy of the developed material model, computational efficiency of the structural Finite Element (FE) analysis is equally important to enable their use in full scale crash analysis simulation models. In particular, efficient approximation and solution methods for the delamination modeling is absolutely crucial to meet today's requirements on virtual development lead times in the automotive industry. For that purpose, we did in a previous paper present a modeling concept which supports laminate failure analyses requiring only one shell element through the thickness, and where arbitrary delamination propagation is accounted for only in areas where it is needed, cf. [11]. This concept can be used as an alternative to the common approach where laminates are modeled with many elements through the thickness (possibly one per ply) connected by cohesive interface elements or similar, cf. Bussadori *et al.* [12] and Greve and Pickett [13], although with the obvious drawback of increased numerical cost. In the current paper, we extend the modeling concept proposed in [11] to also account for intralaminar cracks, still using a single shell element through the thickness. We note the similarities with the work presented by Li *et al.* [14], where they introduced a layerwise method which was is developed to model a composite laminated beam with multiple delaminations and matrix cracks. However, the main difference between the modeling concept proposed herein and the one suggested by Li and co-workers is that, in the present approach there are no additional degrees of freedom (to the original shell degrees of freedom) needed in areas where no cracks appear.

The modeling concept we propose is a direct extension of the idea put forward in [11]. Thus, it is based on the eXtended Finite Element Method (XFEM) [15, 16] which allows for mesh independent representations of discontinuities (*e.g.* inter- and intralaminar cracks) by introducing kinematical enrichments locally in the vicinity of the propagating crack(s). Several researchers before us have successfully utilized the XFEM framework to model failure propagation in composites, cf. *e.g.* Van der Meer *et al.* [17] modeling matrix cracks and delaminations by combining XFEM enhanced solid elements (matrix cracks) and interconnecting classical cohesive elements (delaminations), Ahmed *et al.* [18] proposing a geometrically nonlinear discontinuous solid-like shell element for the modeling of intralaminar crack propagation in thin shell structures and Larsson [19] and de Borst and Rem-

mers [20] modeling arbitrarily located single delaminations. However, in contrast to the above mentioned works, the current modeling concept allows not only one but arbitrarily many delaminations to be included in one and the same shell, at the same time as also any number of intralaminar cracks can be represented. As a consequence, a structural model of a thinwalled laminate can, by using this modeling concept, initially be built up by a single layer of shell elements through the thickness. During loading, the model is then dynamically enriched locally in critical areas where delamination initiation or matrix crack initiation is predicted. Thereby, the computational cost is reduced compared to the more traditional approach based on stacked elements which results in a high number of degrees of freedom even for an undamaged structure.

In the numerical section of this paper we show that the current shell formulation proposed can be utilized to accurately describe the kinematics of a laminate containing multiple inter- and intralaminar cracks. These results thereby indicates that the level of detail in the present approach is such that individual cracks can be analyzed accurately where present. Moreover, the level of detail (and computational cost) of the model is only increased in areas where cracks actually occur, thereby reducing the computational effort required in large scale analyses. Thus, we foresee the use of this modeling concept in analyses in which computational efficiency is of major importance.

2. Initial and deformed shell geometry in terms of convected coordinates

As described in the introduction, the primary focus of the current paper is to propose a modeling concept which kinematically can represent arbitrarily many inter- and intralaminar cracks in a laminate using a single element layer approach, *i.e.* using only one shell element through the thickness of the laminate. For completeness, we present in this section the main aspects of the kinematical shell framework which has been considered in the current work, cf. *e.g.* Larsson *et al.* [21] for details.

The framework consists of three interrelated domains; the inertial Cartesian domain $\mathcal{B}_C$, the undeformed (reference) domain $\mathcal{B}_0$ and the deformed (current) domain $\mathcal{B}$ with pertinent mappings, cf. Figure 1. The initial configuration $\mathcal{B}_0$ of the shell is considered parameterized is in terms of convected (co-variant) coordinates $\boldsymbol{\xi}$ as

$$\mathcal{B}_0 = \{\boldsymbol{X} := \boldsymbol{\Phi}(\boldsymbol{\xi})\}\,, \tag{1}$$

where we introduced the contracted notation $\boldsymbol{\xi} = (\xi^1, \xi^2, \xi^3 = \xi)$ and $\bar{\boldsymbol{\xi}} = (\xi^1, \xi^2)$ for a point in the shell and on the shell mid-surface respectively. Furthermore, the outer boundary of the domains are denoted as Ω with an appropriate subscript depending on configuration. As can be seen from Eq. (1), the mapping $\boldsymbol{\Phi}(\boldsymbol{\xi}) \in \mathcal{B}_0$ maps a point $\boldsymbol{\xi}$ in the inertial Cartesian domain to the corresponding point $\boldsymbol{X}$ in the undeformed reference domain. Associated with the mapping $\boldsymbol{\Phi}$, we also have that the co-variant base vectors $\boldsymbol{G}_i$ in the reference domain are expressed in a general sense as

$$\boldsymbol{G}_i = \boldsymbol{\Phi}_{,i}, \tag{2}$$

where $\bullet_{,i}$ denotes the partial derivative of $\bullet$ with respect to $\xi^i,\ i = 1, 2, 3$.

In a similar fashion, the deformed geometry is described by the deformation map $\boldsymbol{\varphi}(\boldsymbol{\xi}) \in \mathcal{B}$ from the inertial Cartesian frame as

$$\mathcal{B} = \{\boldsymbol{x} := \boldsymbol{\varphi}(\boldsymbol{\xi})\}\,. \tag{3}$$

The pertinent co-variant base vectors in the deformed domain thereby become

$$\boldsymbol{g}_i = \boldsymbol{\varphi}_{,i}. \tag{4}$$

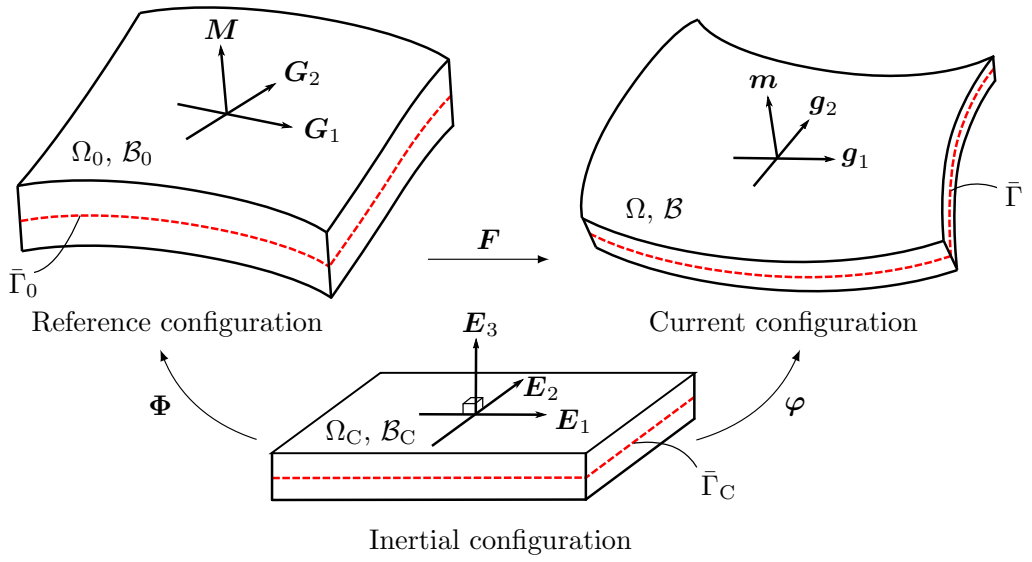

Figure 1: Mappings of shell model defining undeformed and deformed shell configurations relative to the inertial Cartesian frame.

Associated with the deformation from the undeformed to the deformed configuration, we obtain the deformation gradient $\boldsymbol{F}$ as

$$\boldsymbol{F} = \boldsymbol{x} \otimes \boldsymbol{\nabla}_{\mathrm{X}} = \boldsymbol{g}_i \otimes \boldsymbol{G}^i, \quad i = 1, 2, 3 \tag{5}$$

where we have also introduced the contra-variant base vectors $\boldsymbol{G}^i = \partial \xi^i / \partial \boldsymbol{X}$ in the reference configuration which are obtained as

$$\boldsymbol{G}^i = G^{-1}_{ij} \boldsymbol{G}_j \tag{6}$$

using the metric tensor $G_{ij} = \boldsymbol{G}_i \cdot \boldsymbol{G}_j$.

3. A concept for modeling multiple intra- and interlaminar cracks in shells

To describe multiple cracks (inter- and/or intralaminar) within one and the same shell element, the above defined deformation map needs to be extended to allow for displacement discontinuities across the crack interfaces. To do so, we propose to locally enrich the displacement approximation of the shell in the vicinity of any crack in line with the XFEM in the same manner as we did in [11] for modeling of multiple interlaminar cracks. Therefore, we here continue along the same path and extend the previously presented displacement enrichment to also account for intralaminar cracks. First the main results from [11] are summarized, followed by some remarks on the conceptual idea behind the modeling approach. Then we discuss the geometrical description of intralaminar cracks used in the current paper and, finally, we present the kinematical expressions.

3.1. Modeling multiple interlaminar cracks: a summary

In this subsection, only the main equations used to kinematically describe multiple interlaminar cracks are shown, for details see [11]. For this purpose, we consider a laminate built up by n_{ply} plies, each ply defined as lying at a constant distance form the mid-surface. Furthermore, we also consider the existence of a number of interlaminar cracks $\mathrm{N}_{\mathrm{del}}$, where each interlaminar crack k is mathematically represented by the internal surface Γ^{del}_k.

To describe the kinematical representation, we start by considering a split of the placement map into a continuous part and one associated with delaminations (or interlaminar cracks) as follows

$$\boldsymbol{\varphi}(\boldsymbol{\xi}) = \boldsymbol{\varphi}^{\mathrm{c}}(\boldsymbol{\xi}) + \boldsymbol{\varphi}^{\mathrm{del}}(\boldsymbol{\xi}) \tag{7}$$

where $\boldsymbol{\varphi}^{\text{del}}$ consists of a sum of enrichments, one for each interlaminar crack k, according to

$$\boldsymbol{\varphi}^{\text{del}} = \sum_{k=1}^{\text{N}_{\text{del}}} \psi_k^{\text{del}} \boldsymbol{\varphi}_k^{\text{del}}. \tag{8}$$

The enrichment functions ψ_k^{del} are defined as

$$\psi_k^{\text{del}}(\boldsymbol{\xi}) = \psi_k^{\text{del}\xi}(\xi) \cdot \psi_k^{\text{del}\gamma}(\bar{\boldsymbol{\xi}}) \tag{9}$$

with

$$\psi_k^{\text{del}\xi} = \mathcal{H}\left(S_k^{\xi}\right) \tag{10}$$

$$\psi_k^{\text{del}\gamma} = \mathcal{H}\left(S_k^{\gamma}\right) \tag{11}$$

where we introduced the Heaviside function $\mathcal{H}$.

In Eq. (10), $S_k^{\xi}(\xi)$ is a thickness level set (a signed distance function in the thickness direction from a point to the interface k) defined as

$$S_k^{\xi} = \xi - \bar{\xi}_k. \tag{12}$$

Thereby, $S_k^{\xi} = 0$ defines the position through the thickness of the interlaminar crack k. For future purposes, we remark that the material gradient of this level set function correspond exactly to the third contra-variant base vector in the undeformed configuration

$$S_k^{\xi}\big(\xi(\boldsymbol{X})\big) \otimes \boldsymbol{\nabla}_{\text{X}} = \boldsymbol{G}^3, \tag{13}$$

which for most shell theories is identical to the mid-surface normal $\boldsymbol{N}$, cf. also Section 5.

As for $S_k^{\gamma}(\bar{\boldsymbol{\xi}})$, it is defined as an in-plane level set, defined to be positive within the delamination zone of the particular crack k, thereby defining the in-plane extension of the crack ($S_k^{\gamma}(\bar{\boldsymbol{\xi}}) = 0$ on $\partial\Gamma_k^{\text{del}}$, cf. Figure 2). Hence, together $S_k^{\xi}(\xi)$ and $S_k^{\gamma}(\bar{\boldsymbol{\xi}})$ define the corresponding surface Γ_k^{del}.

3.2. Conceptual description of modeling of inter- and intralaminar cracks

We now want to extend the formulation such that we can also model cracks through the plies. To simplify, we assume that all these intralaminar crack surfaces are oriented perpendicular to the mid-surface, in the reference configuration, which means no slanted cracks are considered in the present

formulation. However, as discussed in Subsection 7.1, rather small means are needed to extend the formulation to also handle such inclined intralaminar cracks.

Furthermore, in the discussion below, we will consider the situation that each intralaminar crack does not extend through more than one ply through the thickness of the laminate. Please note that, in general, the formulation will allow for intralaminar cracks which pass through more than one ply. But for clarity reasons, and since cracks in adjacent plies not necessarily coincide in their orientation we restrict the discussion here to the case of cracks in individual plies. However, please note that the case that an intralaminar crack extends through more than one ply can be captured by adding two (or more) enrichments (one for each ply) on top of each other.

3.3. Geometric description of intralaminar cracks using level sets

Returning to the laminate discussed above, we now also introduce a number of $\mathrm{N_{cr}}$ intralaminar cracks (in addition to the interlaminar cracks), each such crack passing through the thickness of one ply having an arbitrary in-plane orientation, cf. Figure 2. In the following, we let each such crack be mathematically represented by a corresponding single crack surface (in the reference configuration) denoted by Γ_l^{cr}, with $l = 1, \dots \mathrm{N_{cr}}$.

To allow the cracks to be active only within one ply, a modified Heaviside enrichment will be used which is zero above and below the ply and one within the ply. Please note that this choice differs from the enrichment used for the interlaminar cracks where a regular Heaviside enrichment was used. To accomplish such ply-individual cracks, we let each intralaminar crack surface be formally described by three level set functions $S_l^{\xi+}(\xi)$, $S_l^{\xi-}(\xi)$ and $S_l^{\gamma}(\bar{\boldsymbol{\xi}})$ defined in $\mathcal{B}_C$, which all will be arguments to the discontinuity enrichment presented in Subsection 3.4. Thereby, $S_l^{\xi+}(\xi) = 0$ and $S_l^{\xi-}(\xi) = 0$ together define the thickness extension of the intralaminar crack l and $S_l^{\gamma}(\bar{\boldsymbol{\xi}}) = 0$ defines the in-plane crack path.

To be specific, the thickness level sets $S_l^{\xi+}(\xi)$ and $S_l^{\xi-}(\xi)$ are the signed distance functions to the top and bottom of the intralaminar crack and can be defined in analogy with Eq. (12) as

$$S_l^{\xi+} = \xi - \bar{\xi}_l^{+}, \tag{14}$$

$$S_l^{\xi-} = \xi - \bar{\xi}_l^{-}. \tag{15}$$

Furthermore, in analogy with Eq. (13), we also have that

$$S_l^{\xi+}\big(\xi(\boldsymbol{X})\big) \otimes \boldsymbol{\nabla}_{\mathrm{X}} = S_l^{\xi-}\big(\xi(\boldsymbol{X})\big) \otimes \boldsymbol{\nabla}_{\mathrm{X}} = \boldsymbol{G}^3. \tag{16}$$

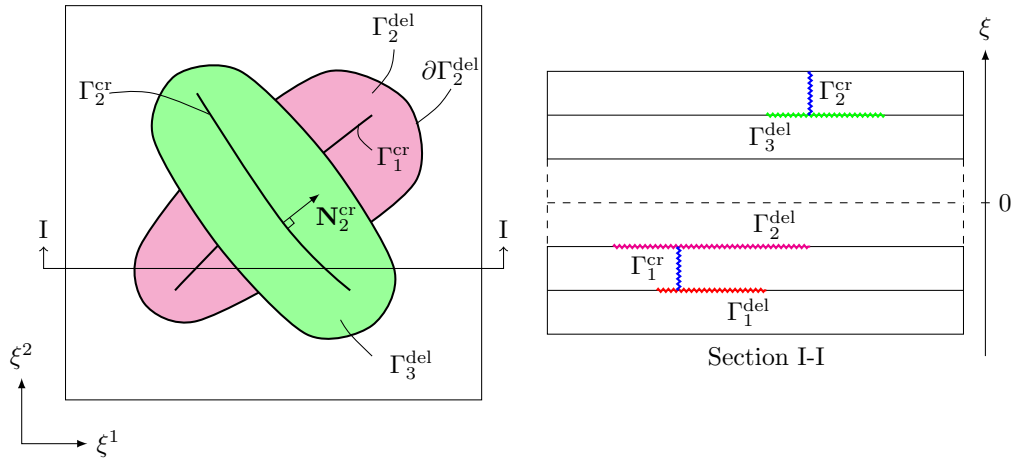

Figure 2: Definition of three interlaminar and two intralaminar crack surfaces with different in-plane and through-the-thickness extensions. The figure also illustrates the boundary $\partial\Gamma_2^{\mathrm{del}}$ of the second delamination surface and the normal $\boldsymbol{N}_2^{\mathrm{cr}}$ of the second intralaminar crack surface.

As for the in-plane level set $S_l^{\gamma}(\bar{\boldsymbol{\xi}})$, it is defined (similar to interlaminar cracks) as the signed distance to the closest point on the in-plane crack path Γ_l^{cr}. By construction, the material gradient of this level set function becomes

$$S_l^{\gamma} \otimes \boldsymbol{\nabla}_{\mathrm{X}} = \boldsymbol{N}_l^{\mathrm{cr}}, \tag{17}$$

where $\boldsymbol{N}_l^{\mathrm{cr}}$ is defined as the normal to Γ_l^{cr}, cf. Figure 2.

3.4. Discontinuity enhanced shell kinematics using the XFEM

As mentioned above, we seek to extend the formulation presented in [11] to also handle intralaminar cracks isolated to one (or several) plies. Therefore, we propose the extension of Eq. (7) according to

$$\boldsymbol{\varphi}(\boldsymbol{\xi}) = \boldsymbol{\varphi}^{\mathrm{c}}(\boldsymbol{\xi}) + \boldsymbol{\varphi}^{\mathrm{del}}(\boldsymbol{\xi}) + \boldsymbol{\varphi}^{\mathrm{cr}}(\boldsymbol{\xi}), \tag{18}$$

where $\boldsymbol{\varphi}^{\mathrm{cr}}$ is defined, analogously with Eq. (8), as a sum of enrichments

$$\boldsymbol{\varphi}^{\mathrm{cr}}(\boldsymbol{\xi}) = \sum_{l=1}^{\mathrm{N_{cr}}} \psi_l^{\mathrm{cr}} \boldsymbol{\varphi}_l^{\mathrm{cr}}. \tag{19}$$

The discontinuous enrichment functions ψ^{cr} introduced for each intralaminar crack is in turn (exactly as for interlaminar cracks) defined as the product between two additional enrichment functions; associated with the thickness direction $\psi_l^{\mathrm{cr}\xi}$ and with the in-plane description of the crack $\psi_l^{\mathrm{cr}\gamma}$ as

$$\psi_l^{\mathrm{cr}}(\boldsymbol{\xi}) = \psi_l^{\mathrm{cr}\xi}(\xi) \cdot \psi_l^{\mathrm{cr}\gamma}(\bar{\boldsymbol{\xi}}) \tag{20}$$

where

$$\psi_l^{\mathrm{cr}\xi} = \mathcal{H}\left(S_l^{\xi-}\right)\left(1 - \mathcal{H}\left(S_l^{\xi+}\right)\right). \tag{21}$$

Thus, $\psi_l^{\mathrm{cr}\xi}$ takes the form of a unit step function from ξ_l^- to ξ_l^+ as illustrated in Figure 3. As a consequence of this particular choice of enrichment, (intralaminar) enrichments in different layers do not couple to each other, although they do contribute to the displacement jump between plies, as discussed in the next subsection. In addition, a shifted enrichment function, cf. *e.g.* [22], is used for the intralaminar crack enrichment $\psi_l^{\mathrm{cr}\gamma}$ ensuring that the enrichment never extends outside the shell elements cut by a crack.

3.4.1. Implications of the proposed enrichments

In Eq. (21), we have used a (modified) Heaviside enrichment which is zero below and above the intralaminar crack while it is one inside the layer, cf. Figure 3c. Thereby, we decouple different intralaminar cracks though the thickness, although with some further implications on the kinematic formulation.

For example, if only an intralaminar enrichment is introduced, as shown in Figure 4, this will create both an intralaminar crack opening and an interlaminar separation (extending to the element boundaries). If this interlaminar separation is unaccounted for, it may result in interpenetration of the plies and one, therefore, need to introduce additional cohesive zones to remove this effect.

To account for this effect in a more straightforward way, we choose to also add interlaminar enrichments whenever we introduce intralaminar enrichments. This allows us, in a natural way, to control the intralaminar crack separation using the cohesive zones introduced for the interlaminar enrichment.

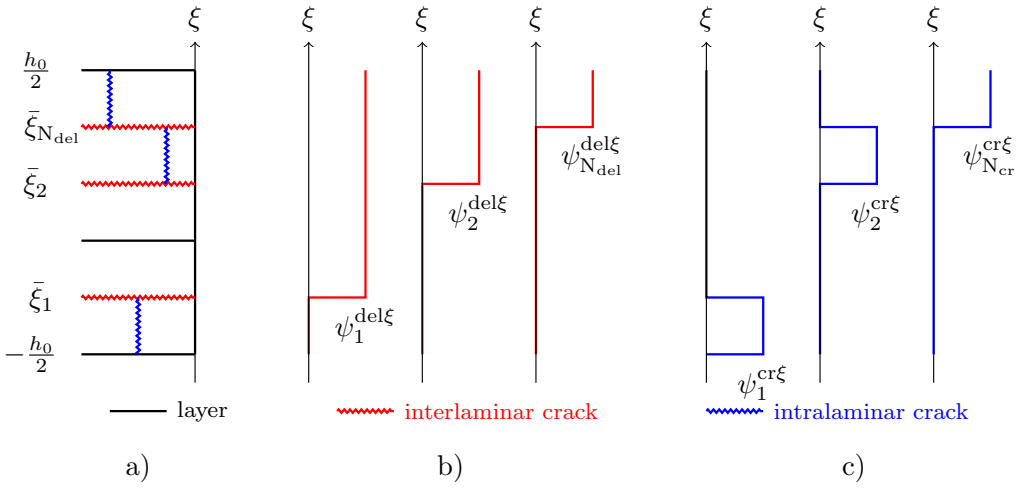

Figure 3: A schematic of the proposed enrichment functions. a) Depicts a laminate (of thickness h_0) with multiple inter- and intralaminar cracks. b) and c) show the enrichment functions $\psi_k^{\mathrm{del}\xi}$ and $\psi_l^{\mathrm{cr}\xi}$ (associated with the thickness direction) for interlaminar and intralaminar cracks respectively.

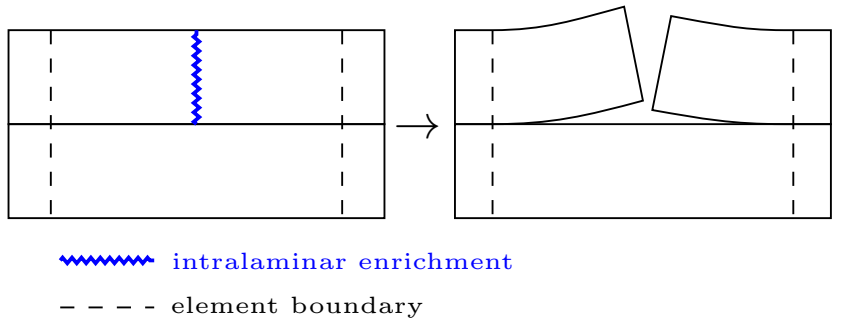

Figure 4: The figure illustrates the effect of a single intralaminar enrichment through one ply. In addition to an intralaminar crack opening it also leads to an interlaminar crack opening.

3.4.2. The discontinuity enhanced deformation gradient

Given the described enrichment of the placement map presented above, we have what is needed to derive a shell element formulation that can handle multiple intra- and interlaminar cracks in one and the same element, which is done for a specialized case (a prototype shell formulation) in Section 5. The procedure however requires the explicit expression for the deformation

gradient $\boldsymbol{F}$ associated with the proposed kinematical representation.

To arrive at the expression for $\boldsymbol{F}$ (which again closely follows [11]), we start by writing it in the following general form:

$$\boldsymbol{F} = \left(\boldsymbol{\varphi}^{\mathrm{c}} + \boldsymbol{\varphi}^{\mathrm{del}} + \boldsymbol{\varphi}^{\mathrm{cr}}\right) \otimes \boldsymbol{\nabla}_{\mathrm{X}} = \boldsymbol{F}^{\mathrm{b}} + \sum_{k=1}^{\mathrm{N_{del}}} \boldsymbol{F}^{\mathrm{del}}_{k\psi} + \sum_{l=1}^{\mathrm{N_{cr}}} \boldsymbol{F}^{\mathrm{cr}}_{l\psi} \tag{22}$$

where $\boldsymbol{F}$ is split into the bounded term $\boldsymbol{F}^{\mathrm{b}}$ and a set of unbounded terms (associated with strong discontinuities) $\{\boldsymbol{F}^{\mathrm{del}}_{k\psi}\}$ and $\{\boldsymbol{F}^{\mathrm{cr}}_{l\psi}\}$.

As for the bounded term, we have that

$$\boldsymbol{F}^{\mathrm{b}} = \boldsymbol{F}^{\mathrm{c}} + \sum_{k=1}^{\mathrm{N_{del}}} \psi^{\mathrm{del}}_k \boldsymbol{F}^{\mathrm{del}}_k + \sum_{l=1}^{\mathrm{N_{cr}}} \psi^{\mathrm{cr}}_l \boldsymbol{F}^{\mathrm{cr}}_l = \boldsymbol{g}^{\mathrm{b}}_i \otimes \boldsymbol{G}^i \tag{23}$$

$$\boldsymbol{F}^{\mathrm{del}}_k = \boldsymbol{\nabla}_{\mathrm{X}} \otimes \boldsymbol{\varphi}^{\mathrm{del}}_k \tag{24}$$

$$\boldsymbol{F}^{\mathrm{cr}}_l = \boldsymbol{\nabla}_{\mathrm{X}} \otimes \boldsymbol{\varphi}^{\mathrm{cr}}_l \tag{25}$$

where the corresponding (bounded) spatial co-variant base vectors $\boldsymbol{g}^{\mathrm{b}}_i$ are defined as

$$\boldsymbol{g}^{\mathrm{b}}_i = \boldsymbol{g}^{\mathrm{c}}_i + \sum_{k=1}^{\mathrm{N_{del}}} \psi^{\mathrm{del}}_k \boldsymbol{g}^{\mathrm{del}}_{ki} + \sum_{l=1}^{\mathrm{N_{cr}}} \psi^{\mathrm{cr}}_l \boldsymbol{g}^{\mathrm{cr}}_{li}. \tag{26}$$

These base vectors are in turn constructed from the base vectors associated with the previously defined placement maps as

$$\boldsymbol{g}^{\mathrm{c}}_i = \boldsymbol{\varphi}^{\mathrm{c}}_{,i}, \tag{27}$$

$$\boldsymbol{g}^{\mathrm{del}}_{ki} = \boldsymbol{\varphi}^{\mathrm{del}}_{k,i}, \tag{28}$$

$$\boldsymbol{g}^{\mathrm{cr}}_{li} = \boldsymbol{\varphi}^{\mathrm{cr}}_{l,i}. \tag{29}$$

In Eq. (22), additional terms arise in the expression for the deformation gradient due to the enrichment functions ψ^{del}_k and ψ^{cr}_l. These additional terms can be written as

$$\boldsymbol{F}^{\mathrm{del}}_{k\psi} = \boldsymbol{\varphi}^{\mathrm{del}}_k \otimes \boldsymbol{\nabla}_{\mathrm{X}}\, \psi^{\mathrm{del}}_k = \{\,\mathrm{cf.}[11]\,\} = \delta^{\mathrm{del}\xi}_k \psi^{\mathrm{del}\gamma}_k [\![\boldsymbol{\varphi}]\!]^{\mathrm{del}}_k \otimes \boldsymbol{G}^3, \tag{30}$$

and

$$\begin{aligned} \boldsymbol{F}^{\mathrm{cr}}_{l\psi} &= \boldsymbol{\varphi}^{\mathrm{cr}}_l \otimes \boldsymbol{\nabla}_{\mathrm{X}}\, \psi^{\mathrm{cr}}_l = \\ &= \delta^{\mathrm{cr}\gamma}_l \psi^{\mathrm{cr}\xi}_l [\![\boldsymbol{\varphi}]\!]^{\mathrm{cr}}_l \otimes \boldsymbol{N}^{\mathrm{cr}}_l + \delta^{\mathrm{del}\xi-}_l \psi^{\mathrm{cr}\gamma}_l \boldsymbol{\varphi}^{\mathrm{cr}}_l \otimes \boldsymbol{G}^3 - \delta^{\mathrm{del}\xi+}_l \psi^{\mathrm{cr}\gamma}_l \boldsymbol{\varphi}^{\mathrm{cr}}_l \otimes \boldsymbol{G}^3. \end{aligned} \tag{31}$$

where we also have introduced the Dirac-delta functions $\delta_k^{\mathrm{del}\xi}$ and $\delta_l^{\mathrm{cr}\xi}$ with the properties:

$$\int_{\mathcal{B}_0} \psi_k^{\mathrm{del}\gamma} \delta_k^{\mathrm{del}\xi} \bullet \, \mathrm{d}\mathcal{B}_0 = \int_{\Gamma_k^{\mathrm{del}}} \bullet \, \mathrm{d}\Gamma \tag{32}$$

and

$$\int_{\mathcal{B}_0} \psi_l^{\mathrm{cr}\xi} \delta_l^{\mathrm{cr}\gamma} \bullet \, \mathrm{d}\mathcal{B}_0 = \int_{\Gamma_l^{\mathrm{cr}}} \bullet \, \mathrm{d}\Gamma. \tag{33}$$

By introducing the general notation $[\![\bullet]\!]$ for a (dis)placement jump, we can write the jump over the interlaminar crack interface Γ_k^{del} as

$$[\![\boldsymbol{\varphi}]\!]_k^{\mathrm{del}} = \boldsymbol{\varphi}|_{\Gamma_k^{\mathrm{del}}}^{+} - \boldsymbol{\varphi}|_{\Gamma_k^{\mathrm{del}}}^{-} \tag{34}$$

and the jump across the intralaminar crack interface Γ_l^{cr} as the difference in placement map on the plus and minus side of the interface as

$$[\![\boldsymbol{\varphi}]\!]_l^{\mathrm{cr}} = \boldsymbol{\varphi}|_{\Gamma_l^{\mathrm{cr}}}^{+} - \boldsymbol{\varphi}|_{\Gamma_l^{\mathrm{cr}}}^{-} = \boldsymbol{\varphi}_l^{\mathrm{cr}}. \tag{35}$$

4. Weak form of momentum balance

To end up with the explicit weak form of the momentum balance associated with the enriched kinematics proposed here, we start from the conventional form which is stated in terms of inertia $\mathcal{W}^{\mathrm{ine}}$, internal work $\mathcal{W}^{\mathrm{int}}$ and external work $\mathcal{W}^{\mathrm{ext}}$ contributions as *Find:* $\boldsymbol{\varphi} \in \mathcal{V}$

$$\mathcal{W}^{\mathrm{ine}}\left(\ddot{\boldsymbol{\varphi}}; \delta\boldsymbol{\varphi}\right) + \mathcal{W}^{\mathrm{int}}\left(\boldsymbol{\varphi}; \delta\boldsymbol{\varphi}\right) = \mathcal{W}^{\mathrm{ext}}\left(\boldsymbol{\varphi}; \delta\boldsymbol{\varphi}\right) \qquad \forall \delta\boldsymbol{\varphi} \in \mathcal{V}_\delta \tag{36}$$

where $\mathcal{V}$ and $\mathcal{V}_\delta$ are function spaces (with sufficient regularity) to which the placement map and its variation, respectively, belong.

The inertia, internal and external virtual work contributions are given (in the reference configuration) as

$$\mathcal{W}^{\mathrm{ine}} = \int_{\mathcal{B}_0} \rho_0 \delta\boldsymbol{\varphi} \cdot \ddot{\boldsymbol{\varphi}} \, \mathrm{d}\mathcal{B}_0 \tag{37}$$

$$\mathcal{W}^{\mathrm{ext}} = \int_{\mathcal{B}_0} \rho_0 \delta\boldsymbol{\varphi} \cdot \boldsymbol{b} \, \mathrm{d}\mathcal{B}_0 + \int_{\Omega_0} \delta\boldsymbol{\varphi} \cdot \boldsymbol{t}_1 \, \mathrm{d}\Omega_0 \tag{38}$$

$$\mathcal{W}^{\mathrm{int}} = \int_{\mathcal{B}_0} \delta\boldsymbol{F} : \boldsymbol{P} \, \mathrm{d}\mathcal{B}_0 \tag{39}$$

where $\boldsymbol{b}$ is the body force per unit volume, $\boldsymbol{t}_1 = \boldsymbol{P}\cdot\boldsymbol{N}$ is the nominal traction vector on the outer boundary Ω_0 with normal $\boldsymbol{N}$, and $\boldsymbol{P}$ is the first Piola-Kirchhoff stress tensor.

To obtain the explicit form of the internal virtual work we note that this contribution can be written using Eqs. (22)–(31) with (39), which yields

$$\mathcal{W}^{\text{int}} = \int_{\mathcal{B}_0} \delta\boldsymbol{g}_i^{\text{b}} \cdot \boldsymbol{P}\boldsymbol{G}^i \,\mathrm{d}\mathcal{B}_0 + \sum_{k=1}^{\text{N}_{\text{del}}} \int_{\Gamma_k^{\text{del}}} \delta[\![\boldsymbol{\varphi}]\!]_k^{\text{del}} \cdot \boldsymbol{t}_{\text{coh}} \,\mathrm{d}\Gamma + \sum_{l=1}^{\text{N}_{\text{cr}}} \int_{\Gamma_l^{\text{cr}}} \delta[\![\boldsymbol{\varphi}]\!]_l^{\text{cr}} \cdot \boldsymbol{t}_{\text{coh}} \,\mathrm{d}\Gamma \tag{40}$$

where $\boldsymbol{t}_{\text{coh}}$ is the (continuous) degrading normal traction on the crack surfaces, introduced as a function of the displacement discontinuity over Γ_k^{del} and Γ_l^{cr} respectively. Furthermore, $\delta[\![\boldsymbol{\varphi}]\!]_k^{\text{del}}$ and $\delta[\![\boldsymbol{\varphi}]\!]_l^{\text{cr}}$ are variations of the discontinuity jumps at each respective crack interface.

5. The prototype shell formulation and its finite element approximation

To validate and exemplify the potential of the proposed modeling concept, we have chosen to apply the proposed kinematical enrichment to a particular shell formulation, identical to what was used when modeling multiple interlaminar cracks only [11]. Thus, we herein only comment on the extensions compared to the previous work, in terms of the additional enrichments introduced.

5.1. The underlying continuous part of the deformation map

As a starting point, the placement map for the initial (undeformed) configuration in Eq. (1) is parameterized as

$$\boldsymbol{\Phi}(\boldsymbol{\xi}) = \bar{\boldsymbol{\Phi}}(\bar{\boldsymbol{\xi}}) + \xi\boldsymbol{M}(\bar{\boldsymbol{\xi}}) \text{ with } \bar{\boldsymbol{\xi}} \in \bar{\Gamma}_0 \text{ and } \xi \in \frac{h_0}{2}[-1,1]. \tag{41}$$

In Eq (41), the mapping $\boldsymbol{\Phi}$ is defined by the mid-surface placement $\bar{\boldsymbol{\Phi}}$ and the outward unit normal director field $\boldsymbol{M}$ defined on the initial mid-surface $\bar{\Gamma}_0$ (with $|\boldsymbol{M}| = 1$) and with h_0 being the initial thickness of the shell. The corresponding co-variant base vectors in the initial configuration thereby becomes

$$\begin{cases} \boldsymbol{G}_\alpha = \bar{\boldsymbol{\Phi}}_{,\alpha} + \xi\boldsymbol{M}_{,\alpha} \\ \boldsymbol{G}_3 = \boldsymbol{M} \end{cases} \tag{42}$$

where the base vectors associated with the tangent plane are indicated with subindex $\alpha = 1, 2$ and where $\boldsymbol{G}^3 = \boldsymbol{G}_3 = \boldsymbol{M}$.

For the continuous part of the deformation map $\boldsymbol{\varphi}^{\mathrm{c}}$ in Eq. (18) the following parametrization of the shell geometry is used

$$\boldsymbol{\varphi}^{\mathrm{c}}(\boldsymbol{\xi}) = \bar{\boldsymbol{\varphi}}^{\mathrm{c}}(\bar{\boldsymbol{\xi}}) + \xi \boldsymbol{m}^{\mathrm{c}}(\bar{\boldsymbol{\xi}}) + \frac{1}{2}\xi^2 \gamma^{\mathrm{c}}(\bar{\boldsymbol{\xi}}) \boldsymbol{m}^{\mathrm{c}}(\bar{\boldsymbol{\xi}}) \tag{43}$$

where the deformed geometry is described in terms of the current mid-surface placement $\bar{\boldsymbol{\varphi}}^{\mathrm{c}}$, the extensible director field $\boldsymbol{m}^{\mathrm{c}}$ and an additional scalar thickness strain γ^{c} (leading to seven degrees of freedom).

The corresponding co-variant base vectors in the deformed configuration, defined in Eq. (27), are then obtained as follows

$$\begin{cases} \boldsymbol{g}^c_\alpha &= \bar{\boldsymbol{\varphi}}_{,\alpha} + \left(\xi + \frac{1}{2}\gamma\xi^2\right) \boldsymbol{m}^{\mathrm{c}}_{,\alpha} + \frac{1}{2}\gamma_{,\alpha}\xi^2 \boldsymbol{m}^{\mathrm{c}}, \ \alpha = 1, 2 \\ \boldsymbol{g}^c_3 &= (1 + \gamma\xi)\, \boldsymbol{m}^{\mathrm{c}} \end{cases} \tag{44}$$

5.2. The discontinuous part of the deformation map

To (kinematically) represent inter- and intralaminar cracks in the current shell formulation, both the mid-surface placement and director must be discontinuous over the crack interfaces. In analogy with [11], where a discontinuous mid-surface placement $\bar{\boldsymbol{\varphi}}^{\mathrm{del}}_k$ and director $\boldsymbol{m}^{\mathrm{del}}_k$ were introduced for each interlaminar crack, we here introduce also the corresponding fields associated with intralaminar cracks as $\bar{\boldsymbol{\varphi}}^{\mathrm{cr}}_l$ and $\boldsymbol{m}^{\mathrm{cr}}_l$ which yields

$$\boldsymbol{\varphi}^{\mathrm{d}} = \sum_{k=1}^{\mathrm{N_{del}}} \psi^{\mathrm{del}}_k \ \left(\bar{\boldsymbol{\varphi}}^{\mathrm{del}}_k(\bar{\boldsymbol{\xi}}) + \xi \boldsymbol{m}^{\mathrm{del}}_k(\bar{\boldsymbol{\xi}})\right) + \sum_{l=1}^{\mathrm{N_{cr}}} \psi^{\mathrm{cr}}_l \ \left(\bar{\boldsymbol{\varphi}}^{\mathrm{cr}}_l(\bar{\boldsymbol{\xi}}) + \xi \boldsymbol{m}^{\mathrm{cr}}_l(\bar{\boldsymbol{\xi}})\right). \tag{45}$$

Note that the second term in Eq. (45) is written in a generic form for the enrichment; however, since a shifted enrichment function is used for this part the discretized version will look different, cf.*e.g.* [22]. The co-variant base vectors associated with the discontinuous motion maps $\boldsymbol{\varphi}^{\mathrm{del}}_{ki}$ and $\boldsymbol{\varphi}^{\mathrm{cr}}_{li}$ takes the following short form

$$\begin{cases} \boldsymbol{g}^{\mathrm{del}}_{k\alpha} = \bar{\boldsymbol{\varphi}}^{\mathrm{del}}_{k,\alpha} + \xi \boldsymbol{m}^{\mathrm{del}}_{k,\alpha} \quad \alpha = 1, 2 \\ \boldsymbol{g}^{\mathrm{del}}_{k3} = \boldsymbol{m}^{\mathrm{del}}_k \end{cases} \tag{46}$$

$$\begin{cases} \boldsymbol{g}^{\mathrm{cr}}_{l\alpha} = \bar{\boldsymbol{\varphi}}^{\mathrm{cr}}_{l,\alpha} + \xi \boldsymbol{m}^{\mathrm{cr}}_{l,\alpha} \quad \alpha = 1, 2 \\ \boldsymbol{g}^{\mathrm{cr}}_{l3} = \boldsymbol{m}^{\mathrm{cr}}_l \end{cases} \tag{47}$$

5.3. The FE approximations

As described in the previous subsection, the shell formulation contains one set of solution fields associated with the continuous motion and several solution fields associated with inter- and intralaminar crack enrichments respectively. The fields associated with the continuous motion and with the interlaminar cracks are approximated over the element in a standard manner, using quadratic $\mathcal{C}^0$-continuous finite element shape functions, as

$$\bar{\boldsymbol{\varphi}}^{\mathrm{c}} \approx \boldsymbol{N}_{\varphi}\hat{\bar{\boldsymbol{\varphi}}}^{\mathrm{c}} \qquad \boldsymbol{m}^{\mathrm{c}} \approx \boldsymbol{N}_{m}\hat{\boldsymbol{m}}^{\mathrm{c}} \qquad \gamma \approx \boldsymbol{N}_{\gamma}\hat{\boldsymbol{\gamma}} \tag{48}$$

$$\bar{\boldsymbol{\varphi}}_k^{\mathrm{del}} \approx \boldsymbol{N}_{\varphi}\hat{\bar{\boldsymbol{\varphi}}}_k^{\mathrm{del}} \qquad \boldsymbol{m}_k^{\mathrm{del}} \approx \boldsymbol{N}_{m}\hat{\boldsymbol{m}}_k^{\mathrm{del}} \tag{49}$$

where $\boldsymbol{N}_{\varphi}$, $\boldsymbol{N}_m$ and $\boldsymbol{N}_{\gamma}$ are the ordinary shape function matrices associated with the interpolation of the mid-surface placement, director field and γ-field, respectively (both continuous and discontinuous fields).

As for the fields associated with intralaminar cracks, these are as above mentioned enriched with a shifted enrichment function, whereby the finite element approximation becomes

$$\psi_l^{\mathrm{cr}\gamma}\bar{\boldsymbol{\varphi}}_l^{\mathrm{cr}} \approx \sum_{i\in I_l}\left(\mathcal{H}(\boldsymbol{X}) - \mathcal{H}(\boldsymbol{X_i})\right) N_i(\boldsymbol{X})\,\hat{\bar{\boldsymbol{\varphi}}}_{l,i}^{\mathrm{cr}} \tag{50}$$

$$\psi_l^{\mathrm{cr}\gamma}\boldsymbol{m}_l^{\mathrm{cr}} \approx \sum_{i\in I_l}\left(\mathcal{H}(\boldsymbol{X}) - \mathcal{H}(\boldsymbol{X_i})\right) N_i(\boldsymbol{X})\,\hat{\boldsymbol{m}}_{l,i}^{\mathrm{cr}} \tag{51}$$

where I_l is the set of nodes enriched with additional degrees of freedom associated with the intralaminar crack l, $N_i(\boldsymbol{X})$ are (again) the standard quadratic and $\mathcal{C}^0$-continuous shape functions and where $\hat{\bar{\boldsymbol{\varphi}}}_{l,i}^{\mathrm{cr}}$ and $\hat{\boldsymbol{m}}_{l,i}^{\mathrm{cr}}$ are the vectors with nodal degrees of freedom for each node i for the enriched mid-surface placement and director field respectively.

In a Galerkin fashion, the test functions for the different fields are then approximated in the same ways as the primary unknowns.

6. Numerical examples for validation of modeling concept

We now seek to illustrate the proposed concept, for modeling of multiple inter- and intralaminar cracks in shell elements. Therefore, two numerical examples are presented. The first example concerns the simulation of a double cantilever beam with one inter- and one intralaminar crack along the beam, with the purpose of verifying the kinematics of the prototype element. Similarly, in the second example the kinematical representation of the current

concept is also verified for a crack that migrates through several layers. The results from the FE simulations have been compared to analytical results obtained using Euler-Bernoulli beam theory with good agreement as will be shown.

In both the examples, a transversely isotropic elastic material model has been used for the mechanical response of all laminae with material parameters reused from [11]. Furthermore, all laminae have a zero degree orientation to facilitate the comparison of the results obtained from the FE analyses with results obtained from analytical beam theory.

E_{L}	126 GPa
$E_{\mathrm{T}} = E_{\mathrm{TT'}}$	10 GPa
$G_{\mathrm{LT}} = G_{\mathrm{TT'}}$	8 GPa
$\nu_{\mathrm{LT}} = \nu_{\mathrm{TT'}}$	0.29

Table 1: Material parameters used for the numerical examples.

6.1. Cantilever beam with one inter- and intralaminar crack

The first example illustrates the capability of the proposed element to handle one interlaminar crack combined with one through-the-thickness crack. The problem considered is a cantilever beam of length $L = 200$ mm, height $h = 3$ mm and width $w = 15$ mm. It consists of two laminae, which are separated by an interlaminar crack (one set of enrichments). In addition, the through-the-thickness crack is represented by two intralaminar cracks (two additional sets of enrichments) that run along the whole length of the beam. This particular setup effectively splits the beam into four smaller (independent) cantilever beams, see Figure 5 for a top view of the beam. The intralaminar cracks are placed at a distance of $b = 6$ mm from the edge thus defining the width of the thinner beams.

The beam is subjected to a prescribed (downwards) vertical displacement in the corner of one of the thinner beams, such that only one of four beam segments should deflect. The beam is modeled using 80 triangular shell elements with quadratic approximation of all the fields.

Euler-Bernoulli beam theory gives that the reaction force necessary to vertically move the free edge a distance of $p = 0.1$ mm is $7.97 \cdot 10^{-3}$ N. The corresponding value obtained from simulation is $7.96 \cdot 10^{-3}$ N which gives a relative error of 0.2%. This verifies that the shell element is capable of

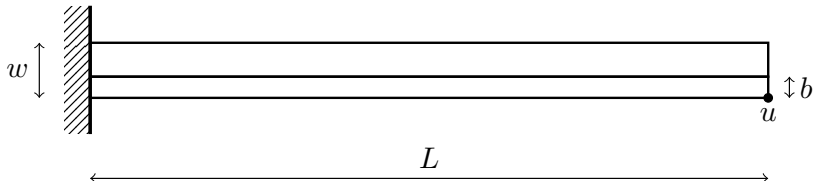

Figure 5: Geometry of the cantilever beam, seen from above, with a through-the-thickness crack along its entire length (at a distance b from the edge).

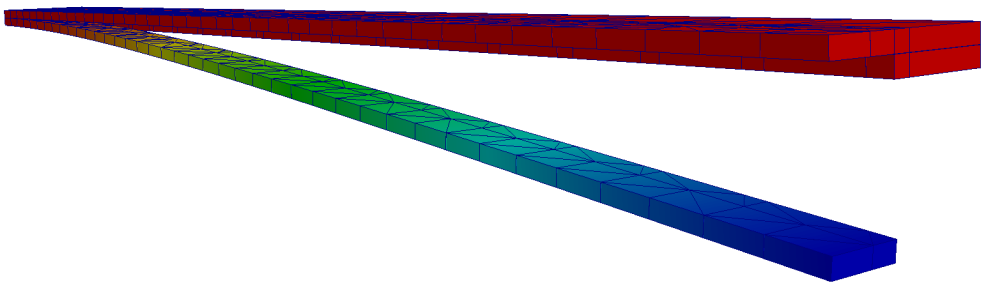

Figure 6: Displacement field for the cantilever beam with intralaminar cracks through both layers combined with an interlaminar crack (magnification factor = 100).

accurately representing the combination of a through-the-thickness crack and one delamination. In Figure 6, the displacement of the beam is shown and it is clear that the expected deformation pattern is recovered. In the figure, also the sub-triangulation of the elements (those cut by a crack) is shown. Please note that, for this particular case a single intralaminar enrichment would have been sufficient, since the top laminae are unloaded.

6.2. Cantilever beam with multiple delaminations and through-the-thickness crack

In the first example, the proposed modeling concept was tested for one interlaminar and two intralaminar cracks. However, more complex crack

patterns can be realized, such as migrating cracks. To illustrate this, we again consider the geometrical setup in the previous example but with the difference that the beam now is composed of seven laminae with a total thickness of 7 mm. In the beam, there are six interlaminar cracks of length $7a$ (except the leftmost which is $5a$) and five intralaminar cracks. Together they form a "staircase" crack pattern where the crack migrates from one layer to the next as illustrated in Figure 7. Furthermore, the beam is modeled using 100 quadratic triangular elements with an approximate element size of 20 mm and is subjected to a constant edge load t at the top of the beam (at its free end) with the magnitude 10 N/m in the vertical direction. This particular setup has been chosen due the simple analytical solution allowing us to verify the kinematics.

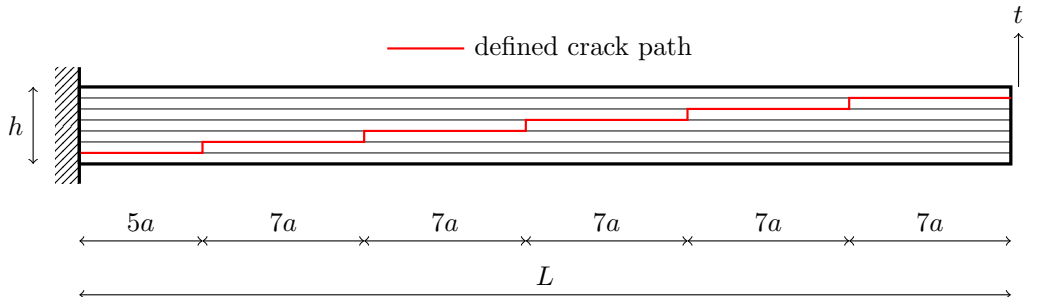

Figure 7: Geometry of the beam with multiple cracks (six interlaminar and five intralaminar) considered in the example in Subsection 6.2. A vertical traction $\boldsymbol{t}$ is applied on the upper edge.

In Figure 8, the deformation pattern obtained from the FE analysis of the beam is shown (in perspective) illustrating the correct deformation pattern. More specifically, by comparing the results obtained in the FE analysis to Euler-Bernoulli beam theory, it is concluded that the difference in calculated maximum beam deflection is less than 0.2 % ($5.349 \cdot 10^{-5}$ m vs. $5.360 \cdot 10^{-5}$ m for beam theory and FE simulation respectively).

7. Conclusions and outlook

In this paper, we propose a generic concept for the modeling of multiple and arbitrarily located intra- and interlaminar cracks in a (potentially curved) laminate. The concept is a direct extension of our work presented in [11], for modeling multiple interlaminar cracks in shells using the XFEM.

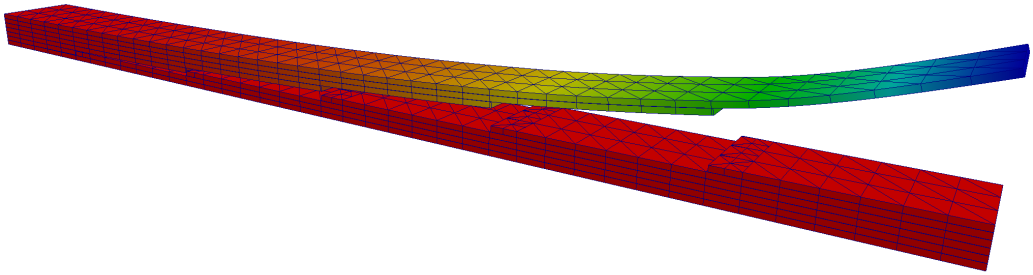

Figure 8: Displacement field for the beam with a migrating crack (magnification factor = 300) considered in the example in Subsection 6.2

.

One main benefit from using the XFEM is that propagating cracks can be kinematically represented independently of the spatial discretization (the finite element mesh) in the FE analysis. Hence, the kinematical representation of the laminate can be adaptively and automatically refined (enriched) whenever a new crack initiates or an existing crack propagates, such that any number of cracks can be realized. This can be achieved independently of the initial spatial representation, which can therefore be rather coarse (in contrast to a mesh containing explicit cracks). As a consequence, a structural model of a thinwalled laminate can, by using this modeling concept, be built up by a single layer of shell elements through the thickness. Thus, no stacking of shell or solid elements, as is traditionally done when analyzing propagation of interlaminar cracks, is needed with this approach. Instead, the structural model is *during* the simulation enriched locally in critical areas where inter- and intralaminar cracks are predicted to initiate or propagate. To be more specific, with this concept any additionally introduced degrees of freedom are kept to a minimum since they are added in relation to the size and number of cracks and their evolution. Thereby, the computational cost may be reduced compared to the more traditional approach (stacked elements) which inevitably results in a high number of degrees of freedom even for an undamaged structure.

To summarize, the proposed modeling concept has the potential of leading to a decrease in virtual development lead times due to the following aspects:

- The shell formulation only involves a local enrichment of the displacement field in the vicinity of the cracks leaving the remaining structure unaffected. Although, the enrichment does lead to a increased bandwidth of the tangent.
- Enrichments do not need to be added *a priori* but are dynamically introduced when and where cracks are predicted to develop.
- The model preparation time for the simulation engineer is reduced, since solid modeling and placement of cohesive zone elements are avoided – this is handled internally within the shell element.

To illustrate and validate the proposed concept, it has been applied to a specific shell element formulation in line with previous developments in [11]. However, we emphasize that the formulation is general and can be applied to other shell formulations as well as solid element formulations.

In the example section of the paper, the resulting shell element kinematics have been verified for a combination of inter- and intralaminar cracks. Based on the results in these examples, we conclude that the proposed modeling concept ca be suitable for simulation of thin-walled structures; in particular for applications where computational efficiency is of major importance.

7.1. Outlook

We have in this contribution presented a modeling concept allowing us to model the progressive development of complex fracture patterns in laminates, using only one shell element through the thickness. This will be beneficial in *e.g.* full scale crash analysis of FRP composites in the automotive industry. There, a typical load scenario would be crushing of beams leading to fracture modes such as delamination and splaying, cf. *e.g.* [6]. To simulate such failure modes would, traditionally, require fine meshing and substantial model preparation time. However, with the proposed modeling concept such analyses can be simplified.

In Figure 9, an example of a laminate containing several intra- and interlaminar cracks are shown illustrating delamination and splaying. Note that, the shown crack configurations are not the result of any simulation but only

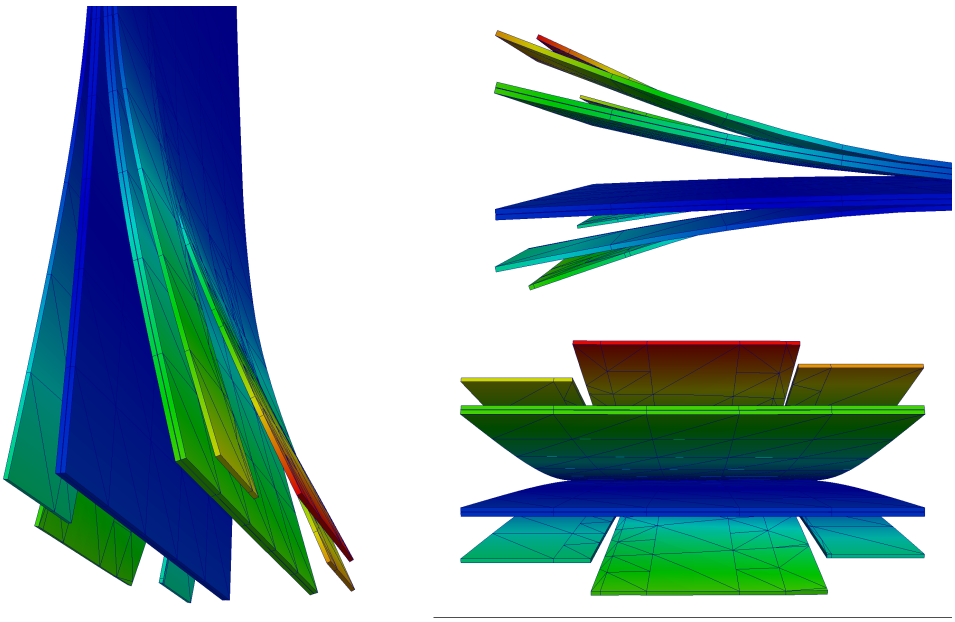

Figure 9: Illustration of a laminate (different views) containing several intra- and interlaminar cracks. Here the laminate is split in the middle by delamination together with additional delamination and splaying of the outer layers.

intended to exemplify what kind of failure modes, on a structural level, that can be represented using the proposed modeling concept.

As a final remark, we would like to clarify that even though we have in this paper restricted the discussion to intralaminar cracks which are perpendicular to the mid-surface of the shell, also inclined cracks could be handled (approximatively) with the same concept. The simplest approach would be to use the same geometrical representation of the cracks as proposed herein, but to allow for the normal $\boldsymbol{N}_l^{\mathrm{cr}}$ to any intralaminar crack l to be oriented with an angle relative to the shell mid-surface, with the angle defined by a suitable crack initiation criterion. This way, the partitioning of the displacement jump across the crack surface in terms of normal and shear contributions would be more realistic.

To simplify the approach, the same positions for the in-plane ply integration points, as if the crack would be normal to the mid-surface, could be used also in the case of an inclined crack. As can be seen in Figure 10, this would lead to a somewhat inaccurate integration of the unbalance forces in the vicinity of the crack since the weights (indicated by the integration point

range in the figure) and positions of the ply integration points would then not be adapted for the case of an inclined crack. But, this effect would be small, also for quite significant angles of the crack inclination (in the figure, the angle is 45°). More important, however, is that the integration points associated with the intralaminar crack need to be positioned along the inclined crack path for an accurate calculation of the displacement jump to be used as the argument in the cohesive zone law.

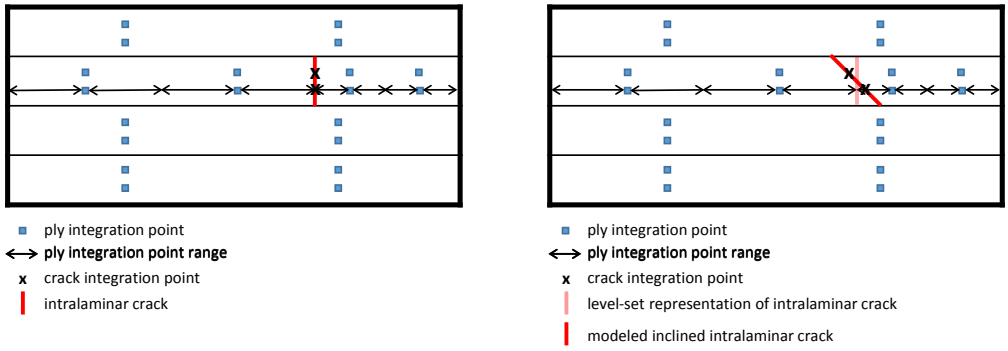

Figure 10: Illustration of how an inclined intralaminar crack could be modeled with the proposed modeling concept in this paper (right). For reference, the idealized case with an intralaminar crack normal to the shell mid-surface is also included (left).

Acknowledgements

The research leading to these results receives funding from the European Community's Seventh Framework Programme (FP7/2007-2013) under grant agreement no. 314182 (the MATISSE project). This publication solely reflects the authors views. The European Community is not liable for any use that may be made of the information contained herein. In addition, funding from the strategic innovation programme LIGHTer provided by VINNOVA is also acknowledged.

References

[1] J.J. Carruthers, A.P. Kettle, and A.M. Robinson. Energy absorption capability and crashworthiness of composite material structures: A review. *Appl. Mech. Rev.*, 51:635–649, 1998.

[2] G.C. Jacob, J.F. Fellers, S. Simunovic, and J.M. Starbuck. Energy absorption in polymer composites for automotive crashworthiness. *J. Compos. Mater.*, 36:813–850, 2002.

[3] H. Hamada, J.C. Coppola, D. Hull, Z. Maekawa, and H. Sato. Comparison of energy absorption of carbon/epoxy and carbon/peek composite tubes. *Composites*, 23:245–252, 1991.

[4] G.L. Farley. Energy absorption of composite materials. *J. Compos. Mater.*, 17:267–279, 1983.

[5] D. Hull. A unified approach to progressive crushing of fibre-reinforced composite tubes. *Compos. Sci. Technol.*, 40:377–421, 1991.

[6] L. Grauers, R. Olsson, and R. Gutkin. Energy absorption and damage mechanisms in progressive crushing of corrugated NCF laminates: Fractographic analysis. *Compos. Struct.*, 110:110 – 117, 2014.

[7] S.T. Pinho, L. Iannucci, and P. Robinson. Physically-based failure models and criteria for laminated fibre-reinforced composites with emphasis on fibre kinking: Part I: Development. *Compos. Part A–Appl. S.*, 37:63–73, 2006.

[8] S.T. Pinho, L. Iannucci, and P. Robinson. Physically-based failure models and criteria for laminated fibre-reinforced composites with emphasis on fibre kinking: Part I: FE implementation. *Compos. Part A–Appl. S.*, 37:766–777, 2006.

[9] P. Maimí, P.P Camanho, J.A Mayugo, and C.G. Dávila. A continuum damage model for composite laminates: Part I - Constitutive model. *Mech. Mater.*, 39:897–908, 2007.

[10] R. Gutkin and S.T. Pinho. Combining damage and friction to model compressive damage growth in fibre-reinforced composites. *J. Compos. Mater. (Published online)*, DOI: 10.1177/0021998314549614, 2014.

[11] J. Brouzoulis and M. Fagerström. An enriched shell element formulation for efficient modeling of multiple delamination propagation in laminates. 126:196–206, 2015.

[12] B.P. Bussadori, K. Schuffenhauer, and A. Scattina. Modelling of CFRP crushing structures in explicit crash analysis. *Compos. Part B–Eng.*, 60:725–735, 2014.

[13] L. Greve and A.K. Pickett. Delamination testing and modelling for composite crash simulation. *Compos. Sci. Technol.*, 66:816–826, 2006.

[14] D. H. Li, Y. Liu, and X. Zhang. An extended Layerwise method for composite laminated beams with multiple delaminations and matrix cracks. *Int. J. Numer. Meth. Eng.*, 101:407–434, 2015.

[15] T. Belytschko and T. Black. Elastic crack growth in finite elements with minimal remeshing. *Int. J. Numer. Meth. Eng.*, 45:601–620, 1999.

[16] N. Moës, J. Dolbow, and T. Belytschko. A finite element method for crack growth without remeshing. *Int. J. Numer. Meth. Eng.*, 46:131–150, 1999.

[17] F.P. van der Meer, L.J. Sluys, S.R Hallett, and M.R Wisnom. Computational modeling of complex failure mechanisms in laminates. *J. Compos. Mater.*, 46:603–623, 2011.

[18] A. Ahmed, F. van der Meer, and L.J. Sluys. A geometrically nonlinear discontinuous solid-like shell element (DSLS) for thin shell structures. *Comput. Method Appl. M.*, 201-204:191–207, 2012.

[19] R. Larsson. A discontinuous shell-interface element for delamination analysis of laminated compos. struct. *Comput. Method Appl. M.*, 193:3173–3194, 2004.

[20] R. de Borst and J.J.C. Remmers. Computational modelling of delamination. *Compos. Sci. Technol.*, 66:713–722, 2006.

[21] R. Larsson, J. Mediavilla, and M. Fagerström. Dynamic fracture modeling in shell structures based on XFEM. *Int. J. Numer. Meth. Eng.*, 86:499–527, 2010.

[22] G. Zi and T. Belytschko. New crack-tip elements for XFEM and applications to cohesive cracks. *Int. J. Numer. Meth. Eng.*, 57:2221–2240, 2003.